Characterization of megahertz X-ray laser beams by multishot desorption imprints in PMMA

VOJTĚCH VOZDA,[1,2,12] (iD) TOMÁŠ BURIAN,[2,3] VĚRA HÁJKOVÁ,[2] LIBOR JUHA,[2,3] HARTMUT ENKISCH,[4] BART FAATZ,[5] MARTIN HERMANN,[4] IWANNA JACYNA,[6] MAREK JUREK,[6] BARBARA KEITEL,[5] DOROTA KLINGER,[6] ROLF LOCH,[5] ERIC LOUIS,[7] IGOR A. MAKHOTKIN,[7] ELKE PLÖNJES,[5] KAREL SAKSL,[3,8] FRANK SIEWERT,[9] RYSZARD SOBIERAJSKI,[6] SEBASTIAN STROBEL,[4] KAI TIEDTKE,[5] SVEN TOLEIKIS,[5] GOSSE DE VRIES,[10] ZDENĚK ZELINGER,[11] AND JAROMÍR CHALUPSKÝ[2,13]

[1] *Charles University, Faculty of Mathematics and Physics, Institute of Physics, Ke Karlovu 5, CZ-121 16 Prague 2, Czech Republic*
[2] *Institute of Physics, Czech Academy of Sciences, Na Slovance 2, 182 21 Prague 8, Czech Republic*
[3] *Institute of Plasma Physics, Czech Academy of Sciences, Za Slovankou 3, 182 00 Prague 8, Czech Republic*
[4] *Carl Zeiss SMT GmbH, Rudolf-Eber-Strasse 2, 73447 Oberkochen, Germany*
[5] *Deutsches Elektronen-Synchrotron DESY, Notkestrasse 85, 22607 Hamburg, Germany*
[6] *Institute of Physics Polish Academy of Sciences, Al. Lotników 32/46, PL-02-668 Warsaw, Poland*
[7] *MESA + Institute for Nanotechnology, University of Twente, The Netherlands*
[8] *Institute of Materials Research, Slovak Academy of Sciences, 040 01 Kosice, Slovak Republic*
[9] *Helmholtz Zentrum Berlin für Materialien und Energie, Albert-Einstein-Str. 15, 12489 Berlin, Germany*
[10] *ASML Netherlands B.V., P.O. Box 324, Veldhoven 5500 AH, The Netherlands*
[11] *J. Heyrovský Institute of Physical Chemistry, Czech Academy of Sciences, Dolejškova 2155/3, 182 23 Praha 8, Czech Republic*
[12] *vozda@fzu.cz*
[13] *chal@fzu.cz*

Abstract: Proper diagnostics of intense free-electron laser (FEL) X-ray pulses is indisputably important for experimental data analysis as well as for the protection of beamline optical elements. New challenges for beam diagnostic methods are introduced by modern FEL facilities capable of delivering powerful pulses at megahertz (MHz) repetition rates. In this paper, we report the first characterization of a defocused MHz 13.5-nm beam generated by the free-electron laser in Hamburg (FLASH) using the method of multi-pulse desorption imprints in poly(methyl methacrylate)(PMMA). The beam fluence profile is reconstructed in a novel and highly accurate way that takes into account the nonlinear response of material removal to total dose delivered by multiple pulses. The algorithm is applied to experimental data of single-shot ablation imprints and multi-shot desorption imprints at both low (10 Hz) and high (1 MHz) repetition rates. Reconstructed response functions show a great agreement with the theoretical desorption response function model.

1. Introduction

The fast development of free-electron laser (FEL) facilities operating in EUV/X-ray regimes contributed to great and significant discoveries which lead to a better understanding of fundamental phenomena taking place in laser-matter interaction and other applications [1]. Many of these processes are highly dependent on laser parameters such as pulse energy, photon energy, spot size

and intensity in the focus, energy distribution across the beam profile, etc. Thus, for the purposes of a proper experimental data analysis, a comprehensive description of the beam is desirable. Several methods employing the Hartmann sensor [2,3], diffractive imaging [4–6], ptychography [7], scanning mask methods [8], lithium fluoride crystals [9,10], and ablation/desorption imprints [11–15] were involved or adapted for the description of short-wavelength high-intensity laser beams.

The trend of the latest FEL development is to provide sources which are able to deliver high-energy pulses at high repetition rate. Facilities like European XFEL [16] and its precursor Free-electron Laser in Hamburg [17] (FLASH) are capable to generate up to 27000 and 4000 pulses per second, respectively, equally distributed in short megahertz (MHz) trains. Linac Coherent Light Source II [18] (LCLS II) promises to deliver up to a million pulses per second in a quasi-continuous mode of operation. The way towards such repetition rates is paved by superconducting technology employed in the linear accelerator. Nevertheless, this progress brings several difficulties whenever the beam is in contact with matter since by entering the megahertz regime we approach time scales typical for heat conduction. The major risk resides in possible local overheating and melting [19] which must be prevented for whatever device or element implemented in the optical beamline, whether it be a beam stopper, solid attenuator, focusing mirror or beam diagnostic tool, for example, an X-ray CCD or ablation imprint target. Thus, damage experiments play a crucial role in the development of new optical components and coatings.

While single pulses can be detected by several beam characterization methods mentioned above, multiple pulses impinging a detector at a high repetition rate represent a real challenge for any beam diagnostics. The method of ablation imprints, which is now routinely used for focus position determination, focused beam profile characterization, focusing optics alignment, etc., is only applicable when the peak fluence of the beam exceeds the ablation threshold of the target material, i.e., it is suitable for exploring intense focused beams in the single-shot regime. In case of moderate- and low-intensity beams, only a small or none part of the beam exceeds the ablation threshold; hence a major part of beam remains unobserved. However, the intensity may still be too high for a safe utilization of sensitive X-ray CCDs. For this purpose a method of desorption imprints in poly(methyl methacrylate) – PMMA was developed [14,20]. PMMA is a photoresist commonly used in EUV lithography the surface of which can be modified even at fluences far below the single-pulse damage threshold (in the so called desorption regime) albeit accumulation of many pulses is required to attain a reasonable imprint contrast. Contrary to ablation, which is by definition a collective volume effect occurring at high intensities, desorption is a moderate surface effect occurring at moderate and low intensity levels [21]. Hence the incident beam profile including its low-intensity wings can be visualized with use of multi-pulse desorption imprints provided that the nonlinear effect of cumulative radiation-induced hardening is taken into account. The method of desorption imprints is applicable, for instance, in visualization of defocused or otherwise attenuated beams.

The aim of this work is to provide a comprehensive tool which allows characterization of short-wavelength MHz beams with use of multi-shot desorption imprints in PMMA. Fundamental principles, conditions of use, as well as a comparison between experimental results obtained by means of desorption and ablation imprinting are summarized in this paper introducing a novel Nonlinear response function recovery (NoReFry) algorithm.

2. Experimental setup

All experimental data were obtained during laser-matter interaction experiments aimed at cumulative (multishot) sub-threshold high-repetition-rate damage testing of EUV/X-ray optical materials. The experiment was conducted at beamline BL2 at the FLASH facility in Hamburg. Targets were irradiated under normal incidence conditions with intense EUV quasi-monochromatic

femtosecond pulses (maximum pulse energy: 100 μJ, central wavelength: 13.5 nm, bandwidth: ~1%, pulse duration: ~100 fs). All exposures were conducted in an ultrahigh vacuum chamber (10^{-7} mbar) dedicated to FEL laser-matter interaction research [22,23]. The incident beam was focused by a carbon-coated elliptical grazing incidence mirror with a focal length of 200 cm. Energy of the pulses was registered by a gas monitor detector (GMD) [24,25]. A GMD calibration factor of (1.18 ± 0.02) and beamline transmission of 68% was taken into account when estimating pulse energy on the target. The temporal structure of trains, delivered by the FLASH facility, is mostly dictated by capabilities of the superconductive linear accelerator and laser-driven injector. In a standard "open-shutter" operation, one second of the beam is composed of ten trains each consisting of 400 pulses separated by 1 μs. This results in 4000 pulses per second, i.e., an effective repetition rate of 4 kHz.

The laser beam was characterized 133 mm downstream from the nominal focus position. In order to validate our results, several different approaches to beam profile measurement were used at this position. Since the maximum achievable pulse energy still exceeded the single-shot ablation threshold of PMMA even at the out-of-focus position, ablation imprints were created first (single-shot operation). Secondly, with use of additional beam attenuation (gas attenuator and thin metallic foils), desorption imprints at low repetition rate (10 Hz) were recorded (one shot per train, 10 shots per second). Finally, the MHz beam was characterized by desorption imprints at high repetition rate (open shutter regime). Ablation imprints were predominantly characterized by Nomarski (DIC – differential interference contrast) microscopy whereas white light interferometry (WLI) was used for a precise 3D scanning of both desorption and ablation imprints.

3. Methods and data analysis

Since the studied X-ray laser beam is non-Gaussian, the fluence scan analysis represents a good tool for its characterization [11,13]. The fluence scan (F-scan) curve displays the fluence as a function of the corresponding iso-fluence contour area within the beam profile. A complex 2D beam profile is thus conveniently reduced into a 1D function. It can be extracted numerically from the beam profile recovered from both the ablation and desorption imprint measured, for example, by means of WLI microscopy (see A.). Alternatively, it can be derived from Nomarski measurements of ablation contours created on PMMA surface. By normalizing the maximum of the F-scan curve to unity, we obtain the so called normalized f-scan curve. The area below the f-scan curve corresponds to the effective area A_{eff}, a beam size parameter which directly relates the peak fluence F_0 and pulse energy E_{pulse} through a relation $F_0 = E_{\text{pulse}}/A_{\text{eff}}$.

3.1. Methods of ablation imprints

Methods of ablation imprints originally emerged from the fact that the transverse $(x - y)$ fluence profile of the incident beam $F(x, y)$ is, under certain circumstances, closely related to a 3D shape $d(x, y)$ of an ablation imprint in PMMA [20,26]. In a limited spectral and dynamic range, the depth profile of the ablated crater is proportional to the logarithm of the fluence profile and, conversely, the fluence profile can be reconstructed from the crater profile via an exponential relation:

$$F(x, y) = F_0 f(x, y) = F_{\text{th}} \exp\left(\frac{d(x, y)}{l_{\text{at}}}\right). \tag{1}$$

Here l_{at} ~193 nm and F_{th} ~ 25 mJ/cm^2 represent experimentally measured absorption length and single-shot ablation threshold fluence of used PMMA targets at the wavelength of 13.5 nm. Peak fluence F_0 represents a normalization factor which can be used to calculate the normalized beam profile $f(x, y)$, fulfilling the normalization condition MAX$\{f(x, y)\} = 1$. An integral of the $f(x, y)$ over the entire plane corresponds to the effective area of the beam. The dynamic range of

direct beam reconstruction is limited from bottom by the ablation threshold being responsible for clipping off low-intensity beam tails. The upper limit is connected with thermal melting leading to a nonlinear deviation from the original exponential relation. Nevertheless, the thermal ablation threshold was not exceeded at the out-of-focus position under study due to a limited output power of the laser. The limitation by thermal ablation is rather relevant in the vicinity of the focus.

In order to significantly extend the dynamic and spectral range of ablation imprinting methods, the fluence scan method was developed [11]. The method uses the fact that the ablation contour left by the beam on the surface ($d(x, y) = 0$) follows an iso-fluence contour corresponding to the threshold fluence level F_{th}, i.e., fulfilling the threshold boundary condition $F(x, y)|_{d=0} = F_0 f(x, y)|_{d=0} = F_{th}$ which naturally follows from Eq. (1). By normalizing the maximum of the fluence profile to unity, we obtain a boundary condition for the normalized profile $f(x, y)|_{d=0} = F_{th}/F_0 = E_{th}/E_{pulse} = 1/p$ where E_{th} stands for the threshold pulse energy. Therefore, by varying the pulse energy E_{pulse} and thus the peak-to-threshold fluence ratio p, we can visualize contours of the beam profile at different levels of maximum. The outer ablation contour is far less sensitive to high-intensity phenomena occurring in the center of the crater which extends the dynamic range of ablation imprinting methods by several orders of magnitude. Different spectral ranges can be reached by a proper choice of the target material.

The fundamental principle of the fluence scan method resides in collecting a large ensemble of ablation imprints at a given distance from the focus and for several attenuation levels. Scanning should be performed in the whole available intensity range, i.e., at least from the ablation threshold of the material up to the full output power of the laser source. By plotting the inverse of the pulse energy $1/E^i_{pulse}$ as a function of the corresponding ablation contour area S_i, we obtain a non-normalized fluence scan curve. Here index i denotes an imprint number. No ablative damage, corresponding to zero contour area ($S = 0$ μm^2), occurs at the threshold pulse energy E_{th}. This value is important to normalize the f-scan curve $f(S_i) = E_{th}/E^i_{pulse}$ from which the effective area can be deduced by numerical integration.

3.2. Methods of desorption imprints

Contrary to ablation imprints, desorption imprints in PMMA [20] do not exhibit the threshold behavior which eliminates truncation of low-intensity beam wings. In order to obtain a good imprint contrast, reasonable number of pulses (typically hundreds) must be accumulated at the target surface and none of the incoming pulses must exceed the ablation threshold. Since desorption imprints require a large number of pulses to be accumulated at a particular spot, good pointing and beam shape stability and consistent laser parameters are of great importance. Using the white-light interferometry (WLI) or atomic force microscopy (AFM), a 3D profile of the imprint can be accurately measured and the incident beam profile can be recovered.

For low accumulated doses, the depth profile $d(x, y)$ of the desorption imprint is nearly proportional to the normalized fluence profile $f(x, y)$ of the beam. As the number of accumulated shots and the total accumulated dose increases, an effect of radiation-induced cross-linking may incur a drop in the single-pulse etch rate since the radiation hardness of PMMA surface rises. This is due to a formation of C=C double bonds networking together individual PMMA chains [27–30]. Consequently, the relation between the maximum crater depth d^{max} and the accumulated dose at the beam maximum ε_0 (peak accumulated dose) deviates from a linear function. Therefore, measurement of the calibration curve $\varepsilon(d)$, an inverse of the response function $d(\varepsilon)$ relating the depth profile and accumulated dose profile as $d(x, y) = d(\varepsilon(x, y))$, is necessary for a correct recovery of the beam profile from the imprint shape. Provided that the pulse-to-pulse fluctuation of the fluence profile $f(x, y)$ is negligible, the deepest point of the crater corresponds to the global maximum of the beam profile. Hence the maximum crater depth can be directly paired with the peak accumulated dose without prior knowledge of the beam profile. Since the beam profile and the effective area is initially unknown, we must use the

fact that the peak fluence F_0^i as well as the peak dose ε_0^i of the i-th pulse can be expressed in terms of pulse energy as: $\varepsilon_0^i = F_0^i/l_{at} = E_{pulse}^i/(A_{eff}l_{at})$. Therefore, the peak accumulated dose $\varepsilon_0 = \sum_i \varepsilon_0^i$ is proportional to the total accumulated energy delivered by individual pulses of energy E_{pulse}^i. Hence, without loss of generality, the calibration curve can be constructed from measured total accumulated energies and the corresponding maximum crater depths derived from WLI measurements. By increasing the number of accumulated pulses, i.e., total accumulated energy, very large dynamic range can be covered. Finally, the beam profile and its effective area can be deduced from calibrated depth profiles.

3.3. Nonlinear response function recovery

The above described approach of $\varepsilon(d)$ curve retrieval omits a large portion of imprint profile data points as it uses only the deepest point. Therefore, a novel Nonlinear response function recovery (NoReFry) algorithm was developed to extract the calibration curve to a much higher accuracy. The algorithm requires several ($N \geq 2$) desorption imprints created by a varied number of pulses, i.e., at different peak accumulated doses. In fact, the algorithm solves the equation $d(x, y) = d(\varepsilon_0 f(x, y))$ to retrieve both the (inverse) response function and fluence profile $f(x, y)$.

The algorithm is based on two assumptions. First, the response function $d(\varepsilon)$ is a monotonically increasing function of accumulated dose which implies that a single value of depth can be uniquely attributed to a single value of dose, irrespective of the single-pulse intensity. Second, an iso-depth contour geometrically coincides with the beam iso-fluence (or, in case of multiple accumulated pulses, iso-dose) contour of the same area. The latter assumption makes it possible to uniquely assign an iso-depth contour of area S to a normalized fluence $f(S)$. Complex 2D problem can be thus reduced to finding a solution of 1D equation $d(S) = d(\varepsilon_0 f(S))$.

The two-dimensional depth profile of the n-th imprint $d_n(x, y)$ can be numerically reshaped and sorted into a monotonically decreasing function $d_n(S; \varepsilon_n)$, the so called depth scan or d-scan, where S indicates an area of a given iso-depth contour and $\varepsilon_n = \varepsilon_{0,n}$ the corresponding peak accumulated dose. Figure 1 shows the principle of the algorithm illustrated with two depth scans $d_1(S; \varepsilon_1)$ and $d_2(S; \varepsilon_2)$ representing two desorption imprints created by different numbers of pulses, i.e., different accumulated doses. Let us denote the maximum depths as $d^{max}_1 = d_1(0; \varepsilon_1) = d_1$ and $d^{max}_2 = d_2(0; \varepsilon_2) = d_2$. These two points can be directly involved in the calibration curve as points $R_1(d_1, \varepsilon_1)$ and $R_2(d_2, \varepsilon_2)$. Furthermore, point $F_1(0, 1)$ can be added for free as the iso-fluence contour area is zero ($S_1 = 0$) and the normalized fluence is $f(0) = 1$ at the beam maximum. More points of the fluence scan and the calibration curve can be obtained by a walk through the composite depth scan plot and sequential application of the 1st and 2nd assumption of the algorithm. In the following we denote the vertex points of the path through the d-scan plot as $P_i(S_k, d_j; \varepsilon_j)$ and the recovered points of the calibration and fluence scan curve as $R_j(d_j, \varepsilon_j)$ and $F_k(S_k, f_k)$, respectively. Starting at point $P_2(S_1, d_2; \varepsilon_2)$ and applying the 1st assumption, we immediately find the point $P_3(S_2, d_2; \varepsilon_2)$ at the same depth and hence at the same dose, but at different iso-depth contour S_2. Consequently, using the 2nd assumption, we can relate the two known peak doses at the point P_3 via an equation $\varepsilon_2 = \varepsilon_1 f(S_2)$ and get the next f-scan point $F_2(S_2, \varepsilon_2/\varepsilon_1)$. Using the 2nd assumption again, we can assign the dose $\varepsilon_3 = \varepsilon_2 f(S_2) = \varepsilon_2^2/\varepsilon_1$ to the point $P_4(S_2, d_3; \varepsilon_3)$ occurring at the identical iso-contour S_2 but at different depth d_3 than the point P_3. This step provides us the next point of the calibration curve $R_3(d_3, \varepsilon_3)$, closes the iteration loop, and brings us back to the initial situation from which another iteration loop can start. In fact, values of the calibration and f-scan curve derived from two d-scans follow a sequence $\varepsilon_j = \varepsilon(d_j) = \varepsilon_2^{j-1}/\varepsilon_1^{j-2}$ and $f_k = f(S_k) = \varepsilon_k/\varepsilon_1 = (\varepsilon_2/\varepsilon_1)^{k-1}$. A larger set of d-scans naturally improves precision of the calibration and f-scan curve as the density of derived points gets much higher. A general mathematical description of the NoReFry algorithm is detailed in B.
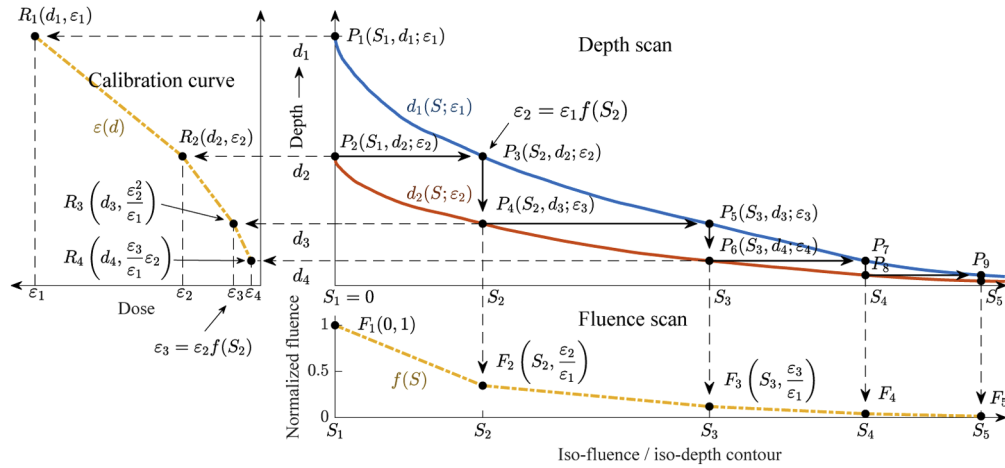
Fig. 1. Principle of the NoReFry algorithm illustrated with two desorption imprints, further explained in the main text.

It should be noted that this new algorithm is applicable not only in nonlinear response recovery of a desorbing target, but also in other situations where the response function monotonically but nonlinearly increases with the accumulated or single-pulse dose, e.g., a fluorescence signal acquired from an exposed LiF crystal [9] or luminescence signal from a saturating Ce:YAG screen [31]. In a very similar manner, the NoReFry algorithm can be applied to a set of ablation imprints in PMMA created by single pulses of a varied energy.

3.4. Response function model

An application of the desorption calibration curve to a real depth profile requires an assumption that the desorbed depth is solely a function of the total deposited dose irrespective of the fluence (intensity) carried by individual pulses. This in other words means that N pulses of equal peak fluence are supposed to incur the same effect as, for example, 2N pulses which are twice weaker. This interaction regime can be designated as deep desorption regime. Evidently, such assumption is valid in a certain fluence range as for large fluences the interaction enters the ablation regime, as reported in [20].

For the purposes of beam profile reconstruction, the recovered calibration or the response curve must be interpolated with a suitable analytic function. Here we use the PMMA desorption model reported by Burian et al. [30]. Since the properties of the desorbing PMMA gradually change during the exposure, the history of the process determines its future. In order to model this non-Markovian process, the authors took into account the radiation hardness as well as a gradual longitudinal shift of the absorption surface (induced by material removal) both increasing with the accumulated dose. The model difference equation is detailed in C. [Eq. (18)]. Assuming the dose increment is small, we can express the model with an integro-differential equation [Eq. (19)] which is, however, still difficult to be solved analytically. Hence we must take a step towards an approximate solution by neglecting the shift of the absorption surface which gives an analytic solution in terms of the exponential integral $E_1(\cdot)$:

$$d(\varepsilon) = l_{\mathrm{at}} \tilde{\kappa}_0^D \left\{ \varepsilon + \frac{\tilde{\Delta}}{\tilde{\gamma}} \left[E_1(\tilde{\gamma}\varepsilon) + \ln(\tilde{\gamma}\varepsilon) - \tilde{\gamma}\varepsilon + \Gamma \right] \right\}. \tag{2}$$

Here the parameter $\Gamma = 0.5772156649$ is the Euler-Mascheroni constant. Even though this approximate model excellently interpolates the response function, we must keep in mind that

the parameters with tildes, i.e., the initial (cold) desorption efficiency rate $\tilde{\kappa}_0^D$, the hardening rate $\tilde{\gamma}$, and the maximum relative decrease of the desorption efficiency rate $\tilde{\Delta}$ may to some extent deviate from the original parameters κ_0^D, γ, and Δ as defined in Eq. (18). A verification fit of the relation (2) to a test dataset generated with use of Eq. (18) confirms a deviation of 5% for $\tilde{\kappa}_0^D$ and $\tilde{\Delta}$ parameters and 20% for $\tilde{\gamma}$ parameter assuming an attenuation length of 193 nm. Applying the inverse of the above formula to the crater profile $d(x, y)$, a relative fluence profile $F(x, y) \sim E(d(x, y,))$ can be recovered.

The model response function for non-thermal single-pulse ablation imprints immediately follows from Eq. (1) as:

$$d(\varepsilon) = l_{at} \ln \left(\frac{\varepsilon}{\varepsilon_{th}} \right), \tag{3}$$

where the dose and threshold dose is related to the local fluence and threshold fluence as $\varepsilon = F/l_{at}$ and $\varepsilon_{th} = F_{th}/l_{at}$, respectively.

4. Results and discussion

Three different operation modes of the FLASH, namely, single-pulse operation, 10-Hz low-repetition rate operation, and 1-MHz high-repetition rate operation, were studied with imprinting methods. Nomarski images of the corresponding imprints are summarized in Figs. 2(a)–(i).
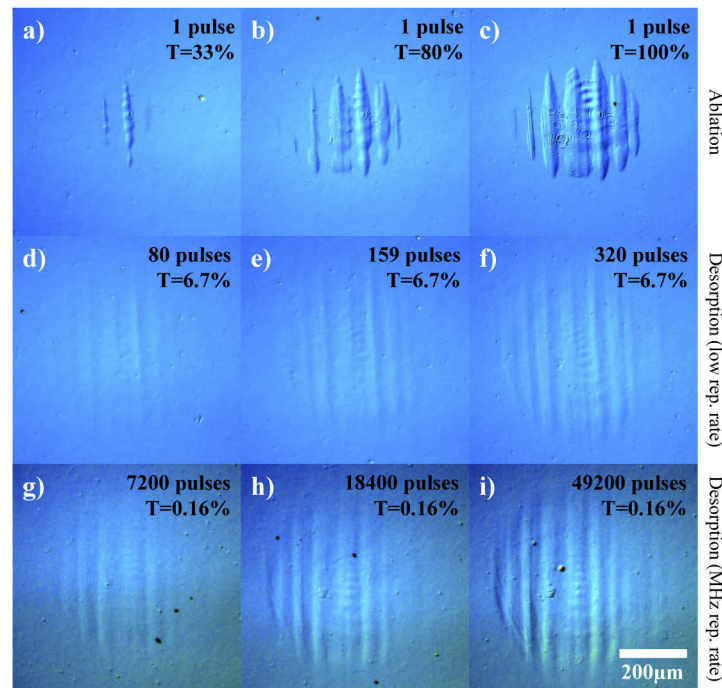

Fig. 2. (a)–(c) Nomarski images of ablation imprints at different beam attenuation levels. (d)–(f) Nomarski images of desorption imprints (low rep. rate) at one attenuation level but for different numbers of accumulated pulses. (g)–(i) Nomarski images of desorption imprints (MHz rep. rate) at one attenuation level but for different numbers of accumulated pulses/trains.

Maximum fluence of a non-attenuated pulse at the position 133 mm downstream from the focus was estimated to be approx. 110 mJ/cm^2. Since this value exceeds the ablation threshold of PMMA, ablation imprints can be to some limited extent used at this moderate-intensity

out-of-focus position even though a major part of the beam remains unseen. In order to obtain the fluence scan, irradiations were done at full power ($T = 100\%$), with the gas attenuator ($T = 80\%$), and with both the gas attenuator ($T = 80\%$) and 203 nm thick zirconium filter (T=41%) resulting in $T = 33\%$. Obtained imprints were analyzed by Nomarski and WLI microscopy. Nomarski images of ablative imprints created at three different attenuation levels in the single-shot mode of operation are shown in Figs. 2(a)–(c). Fine structures such as rings and fringes originate at beamline optics, therefore, their position remains almost unchanged from shot to shot. The intense vertical fringes are speckles originating at small surface imperfections of the grazing incidence focusing mirror.

To visualize the incident beam profile including its wings, desorption imprints at low repetition rate were created. Nomarski micrographs of desorption imprints, where various numbers of single pulses were accumulated at low 10-Hz repetition rate, are shown in Figs. 2(d)–(f). To attenuate the beam below the single-shot damage threshold of PMMA, a combination of two zirconium foils (Zr 296.1 nm + Zr 296.1 nm) was used. Total transmission of this filter combination was measured as T=6.7%. It should be noted that zirconium effectively blocks higher harmonics which are to some extent present in the beam. Depth profiles of desorbed imprints were examined with use of WLI.

In order to enhance the contrast of desorption imprints, the PMMA target was irradiated in the open shutter regime running at the repetition rate of 1 MHz/10 Hz. Various numbers of single trains (each train contains 400 single pulses mutually separated by 1 μs) were accumulated on PMMA surface. In this mode of operation, solid attenuators must not be exposed to the full beam power otherwise the accumulated heat would immediately lead to melting of the metallic foil. Hence the gas attenuator was employed to reduce the FEL output power down to 2.64% of the full power. PMMA exposures were conducted with two configurations of solid attenuators either suppressing or enhancing the relative content of the third harmonic ($\lambda_{3rd} = 4.5$ nm) in the FEL beam. Spectrum of the FEL radiation intrinsically contains an on-axis third harmonic compound since its amplification is allowed during the SASE process. Usually, the energy carried by the 3rd harmonic is low compared to the fundamental compound ($E_{3rd}/E_{1st} \sim 1\%$). However, optical components such as mirrors, gratings and attenuators may considerably vary the T_{3rd}/T_{1st} transmission ratio. In order to quantify the effect of the 3rd harmonic on the desorption process, we employed 101 nm thick aluminium foil to enhance its relative content ($T_{1st} = 4.4\%$, $T_{3rd} = 47\%$) and two niobium foils with thicknesses of 197 nm and 384 nm to reduce its content to negligible values ($T_{1st} = 6.0\%$, $T_{3rd} = 0.001\%$). Total transmission of the fundamental frequency through a combination of gas and solid attenuator was 0.12% for the aluminium foil and 0.16% for niobium foils. Nomarski micrographs of desorption imprints created with use of niobium filters are shown in Figs. 2(g)–(i). Effects of the 3rd harmonic are discussed below.

The NoReFry algorithm was applied to WLI data of the four datasets under study, i.e., to the PMMA ablation (34 profiles), 10-Hz PMMA desorption (5 profiles), and 1-MHz PMMA desorption without (8 profiles) and with (9 profiles) the 3rd harmonic. For brevity we denote these datasets as "ablation", "slow desorption", "fast desorption (no 3rd)", and "fast desorption (with 3rd)", respectively. In total, 2000 iterations were performed for each data ensemble to ensure the convergence. The sum of point variances generated as a byproduct of an averaging process described in the B. was used to track the convergence. The average relative variance of normalized fluence and dose did not exceed 18% and 9%, respectively. Figure 3 displays retrieved fluence scan curves (dense scatter plots) and Nomarski measurements of ablation (iso-fluence) contour areas (solid circles). Figure 4 depicts response function curves as recovered by the code (dense scatter plots), maximum profiles depth as a function of peak dose (circles), and model fits (dashed black lines) utilizing Eqs. (2) and (3).
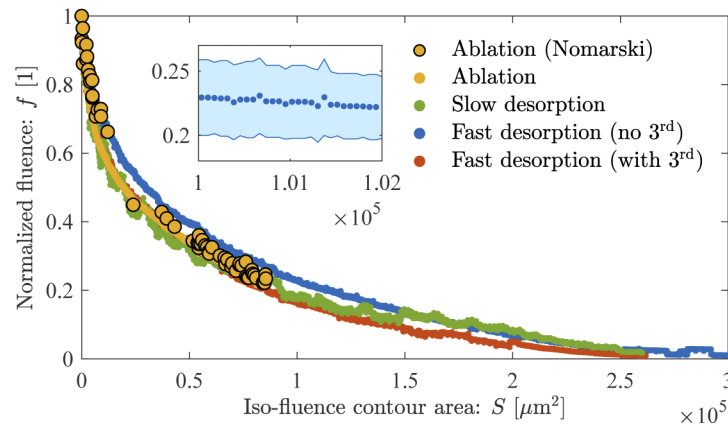
Fig. 3. Fluence scan curves recovered by the NoReFry algorithm for PMMA ablation (orange scatter plot), slow desorption (green scatter plot), fast desorption with (red scatter plot) and without (blue scatter plot) the 3rd harmonic. Orange solid circles depict the Nomarski measurement of ablation contour areas. The inset shows a detail of one of the confidence bands which were not plotted for better readability.
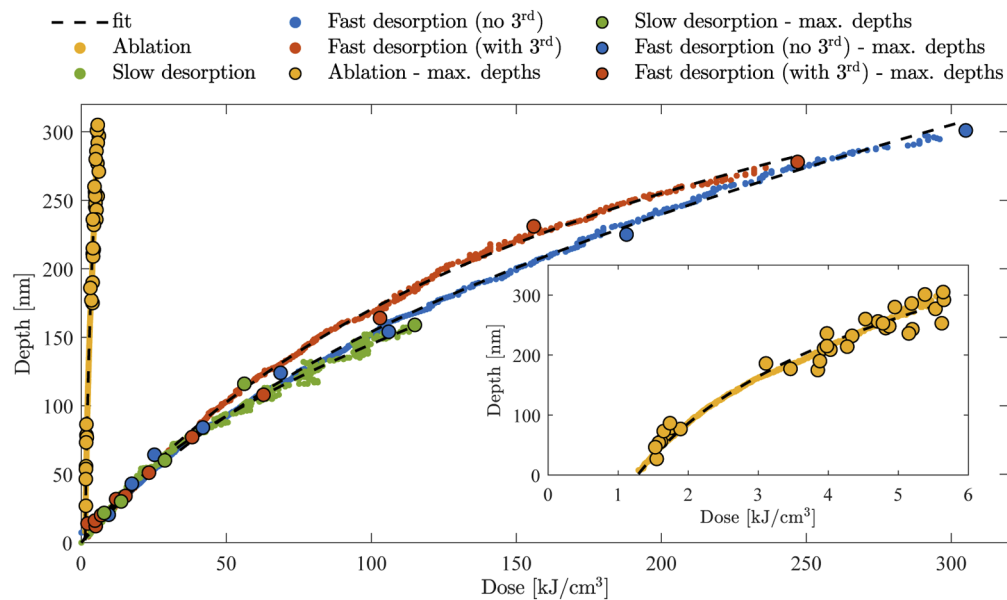

Fig. 4. Response function curves recovered by the NoReFry algorithm for PMMA ablation (orange scatter plot), slow PMMA desorption (green scatter plot), fast PMMA desorption with (red scatter plot) and without (blue scatter plot) the 3rd harmonic. Orange, green, red, and blue solid circles indicate maximum depths of imprints involved in the recovery process. Finally, solid black lines represent model function fits. Inset shows a close-up of the ablation data showing the threshold behavior of the ablation process.

Response function curves in Fig. 4 were recovered in relative units of total accumulated energy. Absolute calibration was done based on known absolute beamline transmission and upon the retrieval of the effective area from each desorption dataset and attenuation length from the ablation dataset. Effective areas and error bars were determined by a numerical integration of

fluence scan curves plotted in Fig. 3 with the aid of the Monte Carlo method: averaged f-scans were randomly varied within a confidence band (see inset in Fig. 3) normally distributed around their curves where the 1-sigma width was in every point determined by a standard deviation of the average. In total 20000 realizations were generated for each f-scan curve. Retrieved effective areas as well as parameters of fitted curves in Fig. 4 are summarized in Table 1.

Table 1. Derived effective areas and fitted model parameters.

		Ablation	Slow desorption	Fast desorption (no 3rd)	Fast desorption (with 3rd)
Effective area:	A_{eff} [μm^2]	$(33900 \pm 2600)^a$	(52500 ± 5300)	(62100 ± 6200)	(48500 ± 5500)
Model parameters Eq. (2)	$\tilde{\kappa}_0^D$ [cm^3/kJ]	—	0.0154	0.0123	0.0133
	$\tilde{\gamma}$ [cm^3/kJ]	—	0.0655	0.0266	0.0195
	$\tilde{\Delta}$ [1]	—	0.816	0.853	1.0
Model parameters Eq. (3)	l_{at} [nm]	192.6	—	—	—
	ε_{th} [kJ/cm^3]	1.28	—	—	—

^{a} An area below an incomplete f-scan curve clipped at the level of f = 0.21.

Fluence scan curves shown in Fig. 3 follow a very similar trend although the effective areas may from various reasons exhibit some differences. Evidently, the effective area as derived from the fast desorption (no 3rd) dataset exceeds the values determined from other desorption data. Depth profiles of representative imprints, as measured by means of white-light interferometry, and normalized beam profiles recovered with use of fitted response functions (calibration curves) are displayed in Fig. 5. A closer look at the recovered (calibrated) beam profiles (Figs. 5(f)–(h)) reveals that the contrast of vertical fringes was reduced and their width was increased in this particular case (Fig. 5(g)) causing an increase of the effective area. The beam profile retrieved from the desorption dataset affected by the 3rd harmonic shows signs of clipping (see Fig. 5(h)) caused by a retainer ring supporting the aluminium attenuator. This makes its effective area the least from all studied cases. The f-scan curve derived from the ablation dataset is only partial due to a small dynamic range limited by the maximum attainable laser power. Therefore, owing to the threshold clipping, the numerical integral below the curve underestimates the beam effective area as it represents only a fraction of the real beam spot area. For the purposes of PMMA ablation threshold evaluation, we assume that effective areas related to ablation and slow desorption datasets are equal since the measurements were done during the same experimental day and the resultant fluence scans are nearly identical within the attainable dynamic range of the ablation imprints method. To demonstrate a good agreement of ablation and desorption imprint methods, contour area measurements, as determined from Nomarski micrographs, are plotted in Fig. 3.

All desorption response functions shown if Fig. 4 exhibit a very similar behavior albeit under distinct beam conditions which validates the reliability and robustness of the method. In the case of slow (10 Hz) and fast (1 MHz) desorption with no 3rd harmonic content, the curves are nearly identical despite a significant difference between repetition rates and beam intensity. This indicates that high-repetition-rate effects, such as local overheating, do not play a crucial role at moderate intensities. Furthermore, material removal in the deep desorption regime exhibits a dominant dose but negligible intensity dependence. Data presented in Fig. 4 and Table 1 confirm that an increased content of higher harmonics can have an effect on the desorption process. Evidently, an enhanced content of the 3rd harmonic causes a steeper rise of the response function (red scatter plot in Fig. 4), i.e., more efficient desorption. This is due to the fact that the total deposited dose involves an unknown additional fraction of energy carried by the 3rd harmonic which is, however, not involved in the absolute dose calibration. Adding this portion of energy would stretch the dose axis of the red scatter plot making the three desorption response functions
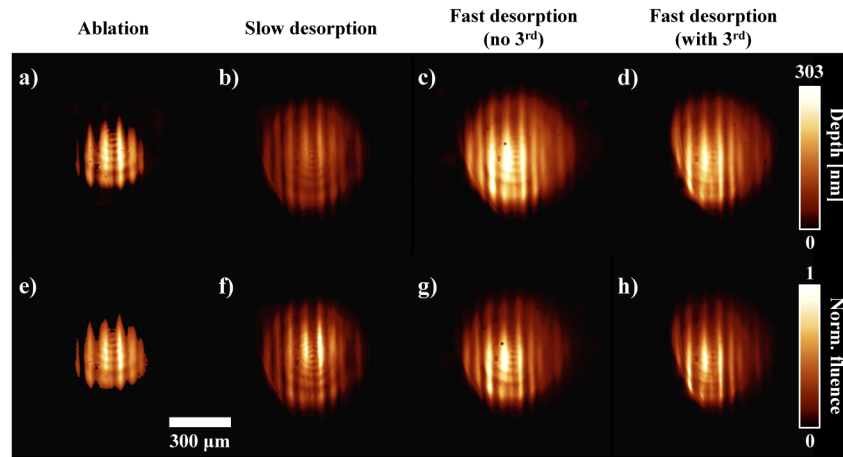
Fig. 5. WLI depth profiles of an ablation imprint (a), low-repetition-rate (slow) desorption imprint (b), high-repetition-rate (fast) desorption imprint without (c) and with (d) 3rd harmonic content. (e)–(h) Corresponding beam profiles recovered using the calibration curves (inverse response functions), retrieved by the NoReFry algorithm and fitted with model functions (2) and (3). All images are in the same measuring scale. Color scales indicate the maximum depth (from 0 nm to 303 nm) and normalized intensity (from 0 to 1) scale for the corresponding row.

nearly overlapped. Another finding on 3rd harmonic effects follows from model function fits summarized in Table 1. Even though the exponential integral model given by Eq. (2) provides rather a qualitative description of the desorption process, the $\tilde{\Delta}$ parameter closer to unity indicates a more efficient radiation-induced hardening. An explanation resides in the attenuation length of 4.5-nm radiation in PMMA ($l_{at,3rd} = 2.63\ \mu m$) penetrating much deeper than the fundamental frequency ($l_{at,1st} = 190.8$ nm) [32] and thus pre-hardening the material. The response function of the ablation process was added to Fig. 4 to visualize its noticeable distinction from desorption response. Inset details the ablation response curve on its own dose scale to emphasize the threshold behavior. Fitting the model function (3) on the ablation data gives an attenuation length of 192.6 nm being in a perfect agreement with the tabulated value [32]. Resultant ablation threshold dose 1.28 kJ/cm^3 corresponds to threshold fluence of 24.6 mJ/cm^2 which is in a good agreement with in-focus measurements [11].

Table 2 shows effective areas and 4-sigma diameters in both horizontal (x) and vertical (y) directions corresponding to recovered beam profiles shown in Fig. 5. Obviously, values derived from the ablation imprint are underestimated due to the clipping. Effective area values listed in Table 2 very well correspond to values summarized in Table 1 which confirms consistency of the results. A comparison of 4-sigma diameters provides a more detailed insight into possible causes of discrepancy between the fast desorption (no 3rd) and other two desorption measurements. Diameters in vertical direction are in a good agreement whereas the horizontal diameter, as determined from the fast desorption (no 3rd) imprint, exceeds the other two indicating an anisotropic beam broadening in the direction perpendicular to speckle fringes. Provided that beamline and beam conditions remained unchanged in both cases of fast desorption, especially, in terms of spatial beam stability, coherence, vibrations of optics, etc., we may attribute the discrepancy to solid attenuators which were the only modified beamline elements. As evident in Fig. 5(h), the beam clipping is responsible for the effective area reduction, in this particular case by less than 10%. On the other hand, fringe contrast lowering observable in Fig. 5(g) can be attributed to small non-uniformities of niobium foils. Introducing local intensity and

wavefront distortions into the beam can result in blurring of fine beam structures and increase of the effective area. This was confirmed with use of an X-ray CCD camera, located far downstream the focus, not only for niobium but also for zirconium foils whereas aluminium foils did not introduce much beam distortions as shown in Fig. 8 (D.). Furthermore, it should be noted that out-of-focus beam parameters, especially the effective area, can be very sensitive to a specific beam and beamline condition, for example, mode structure and position of the source, beam pointing, position of mirrors and apertures. All these properties can to some extent vary on the day-to-day basis. Comparing the beam profiles derived from imprints created on different experimental days, i.e., from slow desorption (Fig. 5(f)) and fast desorption (Fig. 5(g)) imprints, we find distinct positions of beam maxima albeit the overall beam profile is very similar. This indicates a changed beam pointing representing the main contribution to effective area and 4σ-diameter discrepancy between these two cases.

Table 2. Spot sizes (effective areas A_{eff} and 4-sigma diameters $4\sigma_x$ and $4\sigma_y$) determined from recovered beam profiles.

	Ablation[a]	Slow desorption	Fast desorption (no 3rd)	Fast desorption (with 3rd)
A_{eff} [μm^2]	34600	49300	64300	48900
$4\sigma_x$ [μm]	311	419	467	405
$4\sigma_y$ [μm]	303	475	471	461

[a]Beam profile clipped at the normalized fluence level of 0.23.

5. Conclusions

Attenuated defocused megahertz ultrashort EUV beams with intensities below the single-shot ablation threshold of PMMA have been characterized with a method of desorption imprints. Because of the nonlinear dependence between material removal and total deposited doses, the Nonlinear response function recovery (NoReFry) algorithm has been developed, capable of both the material response function and the f-scan curve recovery. Reconstructed beam profiles and fluence scan curves provide a deep and detailed insight into the laser beamline identifying origins of real features often occurring in FEL beams like interference fringes, speckles and beam cropping. Such a detailed knowledge supports conduction of laser-matter interaction experiments utilizing realistic non-Gaussian laser beams. We have also shown that parasitic effects of the 3rd harmonic, intrinsically present in the FEL spectra, can be suppressed by a proper choice of attenuators. It should be noted that the robustness and universality of the NoReFry algorithm enables its application in other beam characterization methods employing sensing elements with a nonlinear response. Moreover, a great reproducibility of the reconstructed response functions obtained under distinct beam conditions will possibly allow using PMMA desorption as an absolutely calibrated dosimeter. More tests with other laser sources at different photon energies and beam conditions are nevertheless needed for a practical utilization.

Appendix A. Extraction of an f-scan curve from the fluence profile

A 2D fluence profile can be converted to a (non)normalized f-scan curve with use of the following algorithm. First, the fluence profile $F(x, y)$ must be sampled onto a regular square (rectangular) grid with the pixel area Δ_S. Second, the corresponding matrix $F_{i,j}$ must be reformed into a vector form F_k and sorted in descending order. This follows from the fact that the fluence scan curve is always a monotonically decreasing function of the iso-fluence contour area. Finally, the sequence $\{S_k, F_k\} = \{k\Delta_S, F_k\}$ is the non-normalized F-scan from which the normalized f-scan curve emerges as $\{S_k, f_k\} = \{k\Delta_S, F_k/F_0\}$.

Appendix B. Nonlinear response function recovery algorithm

The algorithm can be conveniently and generally implemented with use of a matrix formalism for an arbitrary number of d-scan curves. Input data of the code are represented by an ensemble of $N \geq 2$ two-dimensional depth profiles $d_n(x, y)$ and corresponding peak accumulated doses $\varepsilon_{0,n}$. The depth profile can be implemented as a matrix of real dimensions $s_x = R\Delta_x$ and $s_y = C\Delta_y$ where R and C are numbers of rows and columns and Δ_x and Δ_y are dimensions of a single pixel. The profile matrix can be reshaped and sorted in descending order into a monotonically decreasing row vector $\boldsymbol{d}^n$ of length RC where the k-th component of the d-scan vector d_k^n represents a depth of an iso-depth contour with area $S_k = k\Delta_x\Delta_y$. Let us construct a resampled composite depth scan matrix $D_{i,j}$ and its element-by-element inverse $D_{i,j}^{-1}$ out of N depth scan curves sorted in ascending order with respect to $\varepsilon_{0,n}$ as:

$$\forall n \in \{1, \ldots N\}, k \in \{0, \ldots (RC-1)\} :$$

$$D_{i,j} = \begin{cases} \varepsilon_{0,n} \leftrightarrow i = \lfloor \frac{d_k^n}{\Delta_d} \rfloor \wedge j = \rfloor \frac{S_k}{\Delta_S} \wedge i > 0 \\ 0; \text{otherwise} \end{cases} , \tag{4}$$

$$D_{i,j}^{-1} = \begin{cases} \frac{1}{D_{i,j}} \Leftrightarrow D_{i,j} > 0 \\ 0; \text{otherwise} \end{cases} . \tag{5}$$

Here Δ_d and Δ_S are requested sampling intervals for depth and area, respectively, and $\lfloor \cdot \rfloor$ represents the floor function. Within the d-scan matrix each particular d-scan curve is weighted by the corresponding peak accumulated dose. In rare cases, pixels shared by several d-scans are weighted by the maximum value of $\varepsilon_{0,n}$ falling into the pixel since the values are sorted in ascending order. An example of a composite d-scan matrix created from 7 d-scans is shown in Fig. 6.
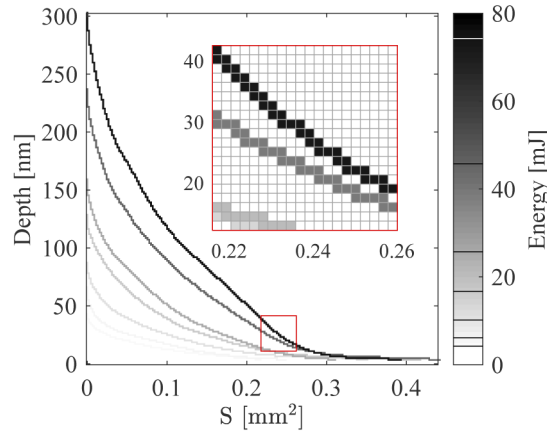

Fig. 6. A composite d-scan matrix constructed from 7 d-scan curves. The only non-zero elements of the matrix are total accumulated energies, proportional to peak accumulated doses $\varepsilon_{0,n}$, at positions defined by the set of $N = 7$ depth scans. The inset shows a section of the d-scan matrix in detail.

In the following, we introduce an average dose $(\varepsilon_i^{\text{avg}})_m$ and f-scan $(f_j^{\text{avg}})_m$ vector where the index m stands for the iteration number and numbers of vector elements correspond to the numbers of rows and columns of the d-scan matrix, respectively. Furthermore, we introduce sum $(\varepsilon_i^{\text{sum}})_m$, $(f_j^{\text{sum}})_m$ and counter $(c_i^\varepsilon)_m$, $(c_j^f)_m$ vectors and auxiliary variables identifying nonzero values in average vectors $(z_i^\varepsilon)_m$, $(z_j^f)_m$ and d-scan matrix $Z_{i,j}^D$. In fact, the first column of the d-scan matrix

$D_{i,0}$ contains peak accumulated doses of all participating imprints which initializes the average dose vector (see the blue curve in Fig. 7 which, according to Eq. (6), represents the initial ansatz of the calibration curve). The complete initialization procedure (the 0th iteration) reads:

$$\left(\varepsilon_i^{\text{avg}}\right)_0 = \left(\varepsilon_i^{\text{sum}}\right)_0 = D_{i,0}$$
$$\text{and} \quad \left(f_j^{\text{avg}}\right)_0 = \left(f_j^{\text{sum}}\right)_0 = 0, \tag{6}$$

$$\left(z_i^{\varepsilon}\right)_0 = \begin{cases} 1 \Leftrightarrow \left(\varepsilon_i^{\text{avg}}\right)_0 > 0 \\ 0; \text{otherwise} \end{cases}$$
$$\text{and} \quad \left(z_j^f\right)_0 = 0, \tag{7}$$

$$Z_{i,j}^D = D_{i,j} D_{i,j}^{-1} = \begin{cases} 1 \Leftrightarrow D_{i,j} > 0 \\ 0; \text{otherwise} \end{cases}, \tag{8}$$

$$\left(c_i^{\varepsilon}\right)_0 = \left(z_i^{\varepsilon}\right)_0$$
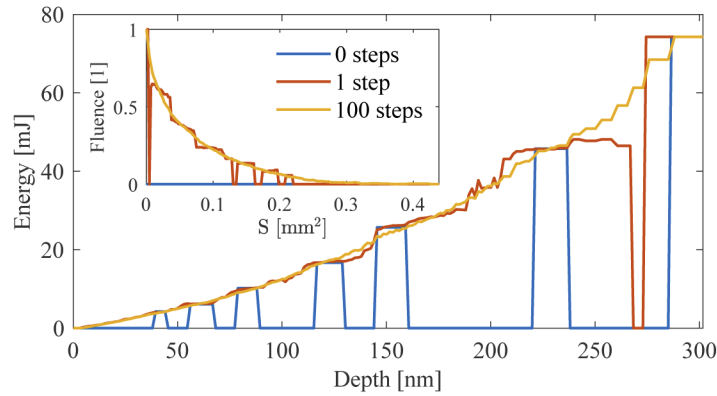$$\text{and} \quad \left(c_j^f\right)_0 = 0. \tag{9}$$

Fig. 7. Calibration curve and fluence scan (inset) after 0, 1, and 100 iterations.

In general, the $(m + 1)$ iteration loop can be implemented as the following ordered list of operations:

$$\left(f_j^{\text{sum}}\right)_{m+1} = \left(f_j^{\text{sum}}\right)_m + \sum_i \left(\varepsilon_i^{\text{avg}}\right)_m D_{i,j}^{-1}, \tag{10}$$

$$\left(c_j^f\right)_{m+1} = \left(c_j^f\right)_m + \sum_i \left(z_i^{\varepsilon}\right)_m Z_{i,j}^D, \tag{11}$$

$$\left(f_j^{\text{avg}}\right)_{m+1} = \begin{cases} \dfrac{\left(f_j^{\text{sum}}\right)_{m+1}}{\left(c_j^f\right)_{m+1}} \dfrac{\left(c_0^f\right)_{m+1}}{\left(f_0^{\text{sum}}\right)_{m+1}} \Leftrightarrow \left(c_j^f\right)_{m+1} > 0 \\ 0; \text{otherwise} \end{cases}, \tag{12}$$

$$\left(z_j^f\right)_{m+1} = \begin{cases} 1 \Leftrightarrow \left(f_j^{\text{avg}}\right)_{m+1} > 0 \\ 0; \text{otherwise} \end{cases}, \tag{13}$$

$$\left(\varepsilon_i^{\text{sum}}\right)_{m+1} = \left(\varepsilon_i^{\text{sum}}\right)_m + \sum_j \left(f_j^{\text{avg}}\right)_{m+1} D_{i,j}, \tag{14}$$

$$\left(c_i^{\mathcal{E}}\right)_{m+1} = \left(c_i^{\mathcal{E}}\right)_m + \sum_j \left(z_j^f\right)_{m+1} Z_{i,j}^D, \tag{15}$$

$$\left(\varepsilon_i^{\mathrm{avg}}\right)_{m+1} = \begin{cases} \dfrac{\left(\varepsilon_i^{\mathrm{sum}}\right)_{m+1}}{\left(c_i^{\mathcal{E}}\right)_{m+1}} \Leftrightarrow \left(c_i^{\mathcal{E}}\right)_{m+1} > 0 \\ 0; \text{otherwise} \end{cases}, \tag{16}$$

$$\left(z_i^{\mathcal{E}}\right)_{m+1} = \begin{cases} 1 \Leftrightarrow \left(\varepsilon_i^{\mathrm{avg}}\right)_{m+1} > 0 \\ 0; \text{otherwise} \end{cases}. \tag{17}$$

Based on the quality of input data and the d-scan matrix, average vectors $(\varepsilon_i^{\mathrm{avg}})_m$ and $(f_j^{\mathrm{avg}})_m$, as defined in (16) and (12), tend to converge to a result within few tens to hundreds iterations as shown in Fig. 7. In order to prevent a drift of the $(f_0^{\mathrm{avg}})_m$ value from unity, a normalization is applied in (12) in each iteration loop. The convergence of the algorithm can be tracked, for example, by evaluating a sum of variances of each averaged value in vectors $(\varepsilon_i^{\mathrm{avg}})_m$ and $(f_j^{\mathrm{avg}})_m$.

Appendix C. Desorption response function model

The process of PMMA desorption induced by a sequence of many X-ray laser pulses can be locally described by the following difference equation [30]:

$$d_{i+1} - d_i = l_{\mathrm{at}} \kappa_0^D \varepsilon_{i+1} \left\{ 1 - \Delta \left(1 + \frac{\exp\left(-\gamma \sum_{n=0}^{i} \varepsilon_n \exp\left(-\frac{d_i - d_{n-1}}{l_{\mathrm{at}}}\right)\right) - 1}{\gamma \sum_{n=0}^{i} \varepsilon_n \exp\left(-\frac{d_i - d_{n-1}}{l_{\mathrm{at}}}\right)} \right) \right\}, \tag{18}$$

where $\varepsilon_0 = 0$ and $d_{-1} = d_0 = 0$. Parameters γ, κ_0^D, and Δ stand for the hardening rate, the initial (cold) desorption efficiency rate and its maximum relative decrease (ranging from 0 to 1), respectively. The summation in the exponential tracks the history of the process up to the i-th pulse which determines an increment of the local depth d_i upon the arrival of the next $(i + 1)$ pulse adding a local dose ε_{i+1}. Assuming the dose increments ε_i are equal and small, we can express the response function with the following integro-differential equation:

$$d'(\varepsilon) = l_{\mathrm{at}} \kappa_0^D \left\{ 1 - \Delta \left(1 + \frac{\exp\left(-\gamma \int_0^{\varepsilon} \exp\left(-\frac{d(\varepsilon) - d(u)}{l_{\mathrm{at}}}\right) du\right) - 1}{\gamma \int_0^{\varepsilon} \exp\left(-\frac{d(\varepsilon) - d(u)}{l_{\mathrm{at}}}\right) du} \right) \right\}. \tag{19}$$

The assumption of no longitudinal shift of the absorption surface with the deposited dose is analogous to a special case of extremely large attenuation length $l_{\mathrm{at}} \gg d$ reducing the exponential in the integral to unity. This reduces the integro-differential Eq. (19) to a solvable differential equation.
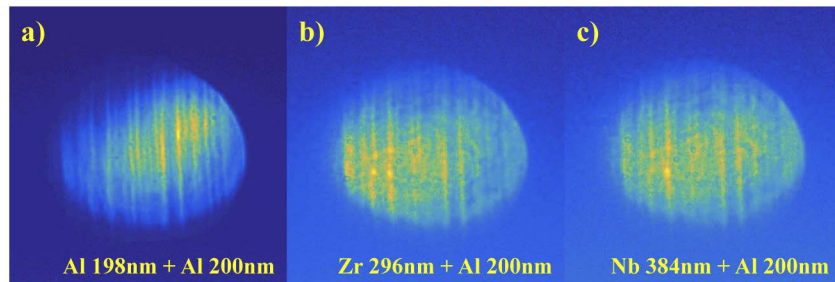
Appendix D. Metallic attenuation foils

Fig. 8. Images of the EUV beam passing through different filter materials as captured by X-ray CCD camera located farther downstream the focus. The beam passing through 198 nm thick aluminium foil (a) evinces only minor signs of scattering and fringe blurring. CCD data for 101-nm Al foil, which was used in the experiment, is not available, however, all tested aluminium foils appear to be of very good quality. Evidently, zirconium 296 nm (b) as well as niobium 384 nm (c) foils introduce small distortions making the fringes blurry. In all three cases an additional Al 200 nm foil was added to match the dynamic range of the CCD. All images are in the same scale.

Disclosures

The authors declare no conflicts of interest.

References

1. S. P. Hau-Riege, *High-Intensity X-rays – Interaction with Matter* (Wiley-VCH Verlag GmbH & Co. KGaA, 2011).
2. S. L. Pape, P. Zeitoun, M. Idir, P. Dhez, J. J. Rocca, and M. François, "Electromagnetic-field distribution measurements in the soft X-ray range: Full characterization of a soft X-ray laser beam," Phys. Rev. Lett. **88**(18), 183901 (2002).
3. B. Flöter, P. Juranić, S. Kapitzki, B. Keitel, K. Mann, E. Plönjes, B. Schäfer, and K. Tiedtke, "EUV Hartmann sensor for wavefront measurements at the Free-electron LASer in Hamburg," New J. Phys. **12**(8), 083015 (2010).
4. H. M. Quiney, A. G. Peele, Z. Cai, D. Paterson, and K. A. Nugent, "Diffractive imaging of highly focused X-ray fields," Nat. Phys. **2**(2), 101–104 (2006).
5. N. D. Loh, D. Starodub, L. Lomb, C. Y. Hampton, A. V. Martin, R. G. Sierra, A. Barty, A. Aquila, J. Schulz, J. Steinbrener, R. L. Shoeman, S. Kassemeyer, C. Bostedt, J. Bozek, S. W. Epp, B. Erk, R. Hartmann, D. Rolles, A. Rudenko, B. Rudek, L. Foucar, N. Kimmel, G. Weidenspointner, G. Hauser, P. Holl, E. Pedersoli, M. Liang, M. S. Hunter, L. Gumprecht, N. Coppola, C. Wunderer, H. Graafsma, F. R. Maia, T. Ekeberg, M. Hantke, H. Fleckenstein, H. Hirsemann, K. Nass, T. A. White, H. J. Tobias, G. R. Farquar, W. H. Benner, S. Hau-Riege, C. Reich, A. Hartmann, H. Soltau, S. Marchesini, S. Bajt, M. Barthelmess, L. Strueder, J. Ullrich, P. Bucksbaum, M. Frank, I. Schlichting, H. N. Chapman, and M. J. Bogan, "Sensing the wavefront of X-ray free-electron lasers using aerosol spheres," Opt. Express **21**(10), 12385 (2013).

6. M. Schneider, C. M. Günther, B. Pfau, F. Capotondi, M. Manfredda, M. Zangrando, N. Mahne, L. Raimondi, E. Pedersoli, D. Naumenko, and S. Eisebitt, "In situ single-shot diffractive fluence mapping for X-ray free-electron laser pulses," Nat. Commun. **9**(1), 214 (2018).

7. A. Schropp, R. Hoppe, V. Meier, J. Patommel, F. Seiboth, H. J. Lee, B. Nagler, E. C. Galtier, B. Arnold, U. Zastrau, J. B. Hastings, D. Nilsson, F. Uhlén, U. Vogt, H. M. Hertz, and C. G. Schroer, "Full spatial characterization of a nanofocused X-ray free-electron laser beam by ptychographic imaging," Sci. Rep. **3**(1), 1633 (2013).

8. H. Yumoto, H. Mimura, T. Koyama, S. Matsuyama, K. Tono, T. Togashi, Y. Inubushi, T. Sato, T. Tanaka, T. Kimura, H. Yokoyama, J. Kim, Y. Sano, Y. Hachisu, M. Yabashi, H. Ohashi, H. Ohmori, T. Ishikawa, and K. Yamauchi, "Focusing of X-ray free-electron laser pulses with reflective optics," Nat. Photonics **7**(1), 43–47 (2013).

9. T. A. Pikuz, A. Y. Faenov, Y. Fukuda, M. Kando, P. Bolton, A. Mitrofanov, A. V. Vinogradov, M. Nagasono, H. Ohashi, M. Yabashi, K. Tono, Y. Senba, T. Togashi, and T. Ishikawa, "Soft X-ray free-electron laser imaging by LiF crystal and film detectors over a wide range of fluences," Appl. Opt. **52**(3), 509 (2013).

10. T. Pikuz, A. Faenov, T. Matsuoka, S. Matsuyama, K. Yamauchi, N. Ozaki, B. Albertazzi, Y. Inubushi, M. Yabashi, K. Tono, Y. Sato, H. Yumoto, H. Ohashi, S. Pikuz, A. N. Grum-Grzhimailo, M. Nishikino, T. Kawachi, T. Ishikawa, and R. Kodama, "3D visualization of XFEL beam focusing properties using LiF crystal X-ray detector," Sci. Rep. **5**(1), 17713 (2016).

11. J. Chalupský, J. Krzywinski, L. Juha, V. Hájková, J. Cihelka, T. Burian, L. Vyšín, J. Gaudin, A. Gleeson, M. Jurek, A. R. Khorsand, D. Klinger, H. Wabnitz, R. Sobierajski, M. Störmer, K. Tiedtke, and S. Toleikis, "Spot size characterization of focused non-Gaussian X-ray laser beams," Opt. Express **18**(26), 27836–27845 (2010).

12. J. Chalupský, P. Bohácek, V. Hájková, S. Hau-Riege, P. Heimann, L. Juha, J. Krzywinski, M. Messerschmidt, S. Moeller, B. Nagler, M. Rowen, W. Schlotter, M. Swiggers, and J. Turner, "Comparing different approaches to characterization of focused X-ray laser beams," Nucl. Instrum. Methods Phys. Res., Sect. A **631**(1), 130–133 (2011).

13. J. Chalupský, T. Burian, V. Hájková, L. Juha, T. Polcar, J. Gaudin, M. Nagasono, R. Sobierajski, M. Yabashi, and J. Krzywinski, "Fluence scan: an unexplored property of a laser beam," Opt. Express **21**(22), 26363 (2013).

14. J. Chalupský, P. Boháček, T. Burian, V. Hájková, S. Hau-Riege, P. Heimann, L. Juha, M. Messerschmidt, S. Moeller, B. Nagler, M. Rowen, W. Schlotter, M. Swiggers, J. Turner, and J. Krzywinski, "Imprinting a focused X-ray laser beam to measure its full spatial characteristics," Phys. Rev. Appl. **4**(1), 014004 (2015).

15. B. Rösner, F. Döring, P. R. Ribič, D. Gauthier, E. Principi, C. Masciovecchio, M. Zangrando, J. Vila-Comamala, G. D. Ninno, and C. David, "High resolution beam profiling of X-ray free electron laser radiation by polymer imprint development," Opt. Express **25**(24), 30686 (2017).

16. T. Tschentscher, C. Bressler, J. Grünert, A. Madsen, A. Mancuso, M. Meyer, A. Scherz, H. Sinn, and U. Zastrau, "Photon beam transport and scientific instruments at the European XFEL," Appl. Sci. **7**(6), 592 (2017).

17. V. Ayvazyan, N. Baboi, I. Bohnet, R. Brinkmann, M. Castellano, P. Castro, L. Catani, S. Choroba, A. Cianchi, M. Dohlus, H. T. Edwards, B. Faatz, A. A. Fateev, J. Feldhaus, K. Flöttmann, A. Gamp, T. Garvey, H. Genz, C. Gerth, V. Gretchko, B. Grigoryan, U. Hahn, C. Hessler, K. Honkavaara, M. Hüning, R. Ischebeck, M. Jablonka, T. Kamps, M. Körfer, M. Krassilnikov, J. Krzywinski, M. Liepe, A. Liero, T. Limberg, H. Loos, M. Luong, C. Magne, J. Menzel, P. Michelato, M. Minty, U.-C. Müller, D. Nölle, A. Novokhatski, C. Pagani, F. Peters, J. Pflüger, P. Piot, L. Plucinski, K. Rehlich, I. Reyzl, A. Richter, J. Rossbach, E. L. Saldin, W. Sandner, H. Schlarb, G. Schmidt, P. Schmüser, J. R. Schneider, E. A. Schneidmiller, H.-J. Schreiber, S. Schreiber, D. Sertore, S. Setzer, S. Simrock, R. Sobierajski, B. Sonntag, B. Steeg, F. Stephan, K. P. Sytchev, K. Tiedtke, M. Tonutti, R. Treusch, D. Trines, D. Türke, V. Verzilov, R. Wanzenberg, T. Weiland, H. Weise, M. Wendt, I. Will, S. Wolff, K. Wittenburg, M. V. Yurkov, and K. Zapfe, "Generation of GW radiation pulses from a VUV free-electron laser operating in the femtosecond regime," Phys. Rev. Lett. **88**(10), 104802 (2002).

18. R. W. Schoenlein, S. Boutet, M. P. Minitti, and A. M. Dunne, "The Linac Coherent Light Source: Recent developments and future plans," Appl. Sci. **7**(8), 850 (2017).

19. R. Sobierajski, I. Jacyna, P. Dluzewski, M. T. Klepka, D. Klinger, J. B. Pelka, T. Burian, V. Hájková, L. Juha, K. Saksl, V. Vozda, I. Makhotkin, E. Louis, B. Faatz, K. Tiedtke, S. Toleikis, H. Enkisch, M. Hermann, S. Strobel, R. A. Loch, and J. Chalupsky, "Role of heat accumulation in the multi-shot damage of silicon irradiated with femtosecond XUV pulses at a 1 MHz repetition rate," Opt. Express **24**(14), 15468–15477 (2016).

20. J. Chalupský, L. Juha, V. Hájková, J. Cihelka, L. Vyšín, J. Gautier, J. Hajdu, S. P. Hau-Riege, M. Jurek, J. Krzywinski, R. A. London, E. Papalazarou, J. B. Pelka, G. Rey, S. Sebban, R. Sobierajski, N. Stojanovic, K. Tiedtke, S. Toleikis, T. Tschentscher, C. Valentin, H. Wabnitz, and P. Zeitoun, "Non-thermal desorption/ablation of molecular solids induced by ultra-short soft X-ray pulses," Opt. Express **17**(1), 208 (2009).

21. R. F. Haglund, "Microscopic and mesoscopic aspects of laser-induced desorption and ablation," Appl. Surf. Sci. **96-98**, 1–13 (1996).

22. R. Sobierajski, J. Krzywinski, A. Andrejczuk, U. Hahn, R. Treusch, M. Jurek, D. Klinger, R. Nietubyć, J. B. Pełka, H. Reniewicz, M. Sikora, and W. Sobala, "Experimental station to study the interaction of intense femtosecond vacuum ultraviolet pulses with matter at TTF1 free electron laser," Rev. Sci. Instrum. **76**(1), 013909 (2005).

23. R. Sobierajski, M. Jurek, J. Chalupský, J. Krzywinski, T. Burian, S. D. Farahani, V. Hájková, M. Harmand, L. Juha, D. Klinger, R. A. Loch, C. Ozkan, J. B. Pełka, K. Sokolowski-Tinten, H. Sinn, S. Toleikis, K. Tiedtke, T. Tschentscher, H. Wabnitz, and J. Gaudin, "Experimental set-up and procedures for the investigation of XUV free electron laser interactions with solids," J. Instrum. **8**(02), P02010 (2013).

24. M. Richter, A. Gottwald, U. Kroth, A. A. Sorokin, S. V. Bobashev, L. A. Shmaenok, J. Feldhaus, C. Gerth, B. Steeg, K. Tiedtke, and R. Treusch, "Measurement of gigawatt radiation pulses from a vacuum and extreme ultraviolet free-electron laser," Appl. Phys. Lett. **83**(14), 2970–2972 (2003).

25. K. Tiedtke, A. Azima, N. von Bargen, L. Bittner, S. Bonfigt, S. Düsterer, B. Faatz, U. Frühling, M. Gensch, C. Gerth, N. Guerassimova, U. Hahn, T. Hans, M. Hesse, K. Honkavaar, U. Jastrow, P. Juranic, S. Kapitzki, B. Keitel, T. Kracht, M. Kuhlmann, W. B. Li, M. Martins, T. Núñez, E. Plönjes, H. Redlin, E. L. Saldin, E. A. Schneidmiller, J. R. Schneider, S. Schreiber, N. Stojanovic, F. Tavella, S. Toleikis, R. Treusch, H. Weigelt, M. Wellhöfer, H. Wabnitz, M. V. Yurkov, and J. Feldhaus, "The soft X-ray free-electron laser FLASH at DESY: beamlines, diagnostics and end-stations," New J. Phys. **11**(2), 023029 (2009).

26. J. Chalupský, L. Juha, J. Kuba, J. Cihelka, V. Hájková, S. Koptyaev, J. Krása, A. Velyhan, M. Bergh, C. Caleman, J. Hajdu, R. M. Bionta, H. Chapman, S. P. Hau-Riege, R. A. London, M. Jurek, J. Krzywinski, R. Nietubyc, J. B. Pelka, R. Sobierajski, J. M. ter Vehn, A. Tronnier, K. Sokolowski-Tinten, N. Stojanovic, K. Tiedtke, S. Toleikis, T. Tschentscher, H. Wabnitz, and U. Zastrau, "Characteristics of focused soft X-ray free-electron laser beam determined by ablation of organic molecular solids," Opt. Express **15**(10), 6036 (2007).

27. E. M. Lehockey, I. Reid, and I. Hill, "The radiation chemistry of poly(methyl methacrylate) polymer resists," J. Vac. Sci. Technol., A **6**(4), 2221–2225 (1988).

28. T. Coffey, S. G. Urquhart, and H. Ade, "Characterization of the effects of soft X-ray irradiation on polymers," J. Electron Spectrosc. Relat. Phenom. **122**(1), 65–78 (2002).

29. C. Peth, F. Barkusky, and K. Mann, "Near-edge x-ray absorption fine structure measurements using a laboratory-scale XUV source," J. Phys. D: Appl. Phys. **41**(10), 105202 (2008).

30. T. Burian, M. Toufarová, J. Chalupský, V. Hájková, V. Vorlícek, S. Hau-Riege, J. Krzywinski, J. D. Bozek, C. Bostedt, A. T. Graf, J. Gaudin, U. F. Jastrow, S. Kapicky, R. A. London, M. Messerschmidt, S. Moeller, R. Sobierajski, K. Tiedtke, M. D. Grazia, T. Auguste, B. Carré, S. Guizard, H. Merdji, N. Medvedev, and L. Juha, "Efficient erosion of an organic polymer irradiated by multiple shots of the X-ray free-electron laser at a fluence below the single-shot ablation threshold: comparing the experiment with two models," Physical Review Applied (accepted for publication).

31. J. Krzywinski, A. Andrejczuk, R. M. Bionta, T. Burian, J. Chalupský, M. Jurek, M. Kirm, V. Nagirnyi, R. Sobierajski, K. Tiedtke, S. Vielhauer, and L. Juha, "Saturation of a Ce:$Y_3Al_5O_{12}$ scintillator response to ultra-short pulses of extreme ultraviolet soft X-ray and X-ray laser radiation," Opt. Mater. Express **7**(3), 665 (2017).

32. B. L. Henke, E. M. Gullikson, and J. C. Davis, "X-ray interactions," At. Data Nucl. Data Tables **54**(2), 181–342 (1993).